Applied Surface Science 709 (2025) 163647

Contents lists available at ScienceDirect

Applied Surface Science

journal homepage: www.elsevier.com/locate/apsusc

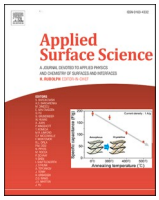

Full Length Article

Synergy of heterojunction engineering and crystal facet regulation to enhance the photocatalytic activity of CQDs/Ni-BDC for CO_2 reduction

Guanhong Lu [a,b], Xiao Wang [a], Xinge Li [a], Yan Wang [a], Gansheng Shi [a], Xiaofeng Xie [a], Jing Sun [a,*]

[a] State Key Lab of High Performance Ceramics and Superfine Microstructure, Shanghai Institute of Ceramics, Chinese Academy of Sciences, 585 Heshuo Road, Shanghai 201899, China

[b] University of Chinese Academy of Sciences, 19 (A) Yuquan Road, Beijing 100049, China

ARTICLE INFO

Keywords:
CQDs/Ni-BDC
photocatalytic CO_2 reduction reaction (pCO_2RR)
Heterojunction
Crystal facet regulation

ABSTRACT

In the field of photocatalysis, heterojunction engineering and crystal surface regulation have emerged as critical research areas, offering effective strategies to significantly enhance the photocatalytic performance of semiconductor materials. However, the synergy between these two strategies in metal–organic frameworks (MOFs) has been scarcely reported. In this study, a series of CQDs/Ni-BDC (BDC: terephthalic acid) hybrids were prepared by a simple one-step ultrasonic method. The result of the photocatalytic CO_2 reduction reaction (pCO_2RR) and control experiments revealed that 0.45 %CQDs/Ni-BDC exhibited the highest photocatalytic CO_2 reduction performance among all as-prepared photocatalysts, with a 0.248 $mmol{\cdot}g^{-1}{\cdot}h^{-1}$ CO evolution rate, a 1.338 $\mu mol{\cdot}g^{-1}{\cdot}h^{-1}$ CH_4 evolution rate and a CO electron selectivity of 97.89 %. The CO yield rate of 0.45 %CQDs/Ni-BDC was 3.2 times higher than that of pure Ni-BDC. XRD results revealed that Ni-BDC predominantly exposed the (100) crystal facet after CQDs modification. PL and electrochemical tests demonstrated that the construction of the CQDs/Ni-BDC heterojunction was successfully prepared to facilitate efficient carrier separation and migration, leading to an increased photoelectron lifetime.

1. Introduction

The sustainable development of human society is impeded by two major challenges, namely environmental pollution and energy crisis. Carbon dioxide, as a prevalent greenhouse gas, is a major contributor to environmental issues such as global warming [1–6]. Among numerous technologies for capture/conversion of CO_2, photocatalytic CO_2 reduction reaction (pCO_2RR) technology has attracted considerable attention due to its cost effectiveness, mild reaction conditions, and convenience of operation. Photocatalytic carbon dioxide reduction utilizes solar energy to convert CO_2 and H_2O into CO, CH_4 and other valuable carbon-based chemical fuels, providing potential solutions to both the greenhouse effect and energy problems[7–12]. However, this technology is currently limited by low conversion rates[13,14], poor selectivity [15,16], and catalyst deactivation[17]. Therefore, the synthesis of efficient and stable catalysts continues to be a primary focus in ongoing research[18–22].

Metal-organic frameworks (MOFs), including NH_2-UiO-66(Zr)[23], NH_2-MIL125(Ti)[24], Fe/Ni-MOF[25], MIL-127(Fe)[26], have been extensively used in pCO_2RR due to their inherent structural flexibility, significantly larger surface area, exceptional porosity, and tunable optical properties, However, the rapid recombination of photogenerated electron-hole pairs resulted in a low light harvesting efficiency of MOFs during the pCO_2RR. Compared to 3D bulk MOFs, 2-dimensional nanosheet MOFs, were considered to exhibit rapid mass transfer and superior electron transfer attributed to their nanometer thickness[27]. Zhong et. al[28] synthesized three kinds of 2D Ni-based MOFs to demonstrate that an increased number of unsaturated Ni-oxo catalytic sites can facilitate the photogenerated electron transfer, thereby promoting CO yield in pCO_2RR. Meanwhile, heterojunction engineering through combination of diverse types of semiconductors or other composition (e.g. carbon materials, noble metals) remains applicable to MOFs. In the study by Wang et al. [29], a homologous heterojunction photocatalyst, NiO (111)/Ni-BDC, was designed by in-situ growth of Ni-BDC on NiO(111) with H_2BDC acting as the etchant. The catalyst was employed for the reduction of carbon dioxide (CO_2) into methane (CH_4) and carbon

* Corresponding author.
E-mail address: jingsun@mail.sic.ac.cn (J. Sun).

https://doi.org/10.1016/j.apsusc.2025.163647
Received 3 April 2025; Received in revised form 15 May 2025; Accepted 27 May 2025
Available online 1 June 2025

monoxide (CO). Furthermore, the regulation of crystal facets has emerged as a promising strategy to enhance the photocatalytic activity of metal–organic frameworks (MOFs). A 2D Ni-based MOF (Ni-BDC) with abundant (100) facets has been reported, which was achieved by adjusting the ratio of Ni ions to organic ligand. The material exhibited enhanced photocatalytic CO_2 to CO capacity in comparison to the (010) facet due to the increased exposure of unsaturated Ni^{2+}[29]. Consequently, the co-optimization of heterojunction engineering and crystal facet regulation in 2D MOFs emerges as a prospective approach.

Carbon quantum dots (CQDs)[30,31] represent a novel variety of carbon-based nanomaterials that have been identified as efficacious compositions for the fabrication of heterojunction constructions integrating with semiconductor materials, including MOFs. This is attributable to their rapid electron-accepting and −transferring properties [32]. In addition, it has been previously reported that CQDs could enhance the catalytic performance of inorganic semiconductor materials through the regulation of their crystal facets. For instance, CQDs/BiOBr composites exhibited a gradual increase in diffraction peak intensity at the (100) crystal facet with in increasing content of CQDs[33]. Therefore, CQDs were anticipated to accomplish both heterojunction construction and crystal facet regulation of MOFs.

In this work, carbon quantum dots (CQDs) were used to obtain the rich (100) crystal facet in Ni-BDC and to form a CQDs/Ni-BDC heterojunction construction by a simple one-step method. XRD analysis results revealed that Ni-BDC was oriented along (100) crystal facet after CQDs modification, and that the crystallinity was significantly improved. Furthermore, CQDs/Ni-BDC exhibited a superior pCO_2RR performance with a higher CO yield rate and CO selectivity compared to Ni-BDC. Electrochemical and fluorescence spectra (PL) results demonstrated that the incorporation of CQDs represented an effective strategy for enhancing the separation efficiency of photogenerated electron-hole pairs, thereby leading to a significant improvement in photocatalytic performance. The multi-cycling pCO_2RR test results demonstrate the superior structural stability of CQDs/Ni-BDC in the acetonitrile/triethanolamine/water test system under Xenon light.

2. Experimental Section

2.1. Materials

All chemicals and reagents were obtained from suppliers and were directly used without further purification. Nickel (II) chloride hexahydrate ($NiCl_2{\cdot}6H_2O$, >98 %), terephthalic acid (H_2BDC, >99 %), N, N-dimethylacetamide (DMA, AR), acetonitrile (MeCN, AR) and triethanolamine (TEOA, AR) was purchased from Shanghai Titan Scientific Co., Ltd. High-purity CO_2 (99.999 %) was purchased from Shanghai Wetry Standard Gas Analysis Technology Co., Ltd.

2.2. Synthesis of Ni-BDC

Ni-BDC was synthesised by a simple ultrasound method referring to a previous report[34]. 0.75 mmol H_2BDC was dissolved in a mixed solution that included 32 mL DMF, 2 mL deionized water and 2 mL ethanol. Then, 0.75 mmol $NiCl_2{\cdot}6H_2O$ and 0.8 mL TEA were added in sequence to the mixture to obtain a colloidal suspension. Subsequently, the suspension was ultrasonicated for 8 h (53 kHz). Ni-BDC was collected by centrifugation, washed with DMF and H_2O 3 times and dried by vacuum freeze-drying for 12 h.

2.3. Synthesis of CQDs

CQDs was synthesised basing on a previous report[31]. Briefly, Urea (1.0 g) and citric acid (1.0 g) were dissolved in 15 ml deionized water and then was transferred into 30 ml Teflon autoclave at 180 °C for 6 h. The resulting dark green solution was centrifugated at 10000 rpm for 30 min to remove the lager particles after cooling down to room temperature. The upper layer solution obtained from centrifugation was dried at 80 °C for 12 h to obtain black CQDs solid. Then CQDs was dissolved in deionized water to obtain a 0.5 mg/mL solution for subsequent synthesis.

2.4. Synthesis of CQDs/Ni-BDC by a one-step ultrasonic method:

CQDs solution (0.5 mg/mL) of 0.5, 1.0, 1.5 and 2.0 mL were separately added in the precursor solution for preparing a serial of CQDs/Ni-BDC hybrids, and the obtained samples were named as x CQDs/Ni-BDC (x = 0.15 %, 0.30 %, 0.45 % and 0.60 %, x represents the mass percentage of the added CQDs to the theoretical yield of Ni-BDC). 0.15 % CQDs/Ni-BDC is utilized as an illustrative example. 0.5 mL CQDs solution and 0.75 mmol H_2BDC were dissolved in a mixed solution that included 32 mL DMF, 1.5 mL deionized water and 2 mL ethanol. Then, 0.75 mmol $NiCl_2{\cdot}6H_2O$ and 0.8 mL TEA were added in sequence to the mixture to obtain a colloidal suspension. The subsequent synthesis procedures aligned with the methodology employed for Ni-BDC synthesis. Notably, the amount of water added during the synthesis of each sample was maintained at 2 mL.

2.5. Synthesis of CQDs/Ni-BDC by a two-step method:

In the initial step, Ni-BDC was synthesized following the aforementioned method. In the subsequent step, the entirety of the Ni-BDC obtained in a single batch was dispersed in 32 mL of DMF. Subsequently, 1.5 mL of CQDs solution (0.5 mg/mL) was added, and the mixture was subjected to ultrasonication for 8 h. The washing and drying conditions were in accordance with the preparation method of Ni-BDC.The resultant sample was designated as 0.45 %CS-2.

2.6. Characterization

The crystalline structure of as-prepared photocatalysts was investigated by powder X-Ray diffractometer (PXRD, Bruker D8 ADVANCE, Germany) using Cu Kα with the scanning rate of 5°/min. The morphology of samples was measured by a transmission electron microscope (TEM, JEM-2100F, Japan). X-ray photoelectron spectra (XPS) were carried out on a spectrometer (Microlab 310F Scanning Auger Microprobe, VG SCIENTIFIC LTD) with a monochromatic Al-Ka (1486.6 eV) X-ray source. The UV–vis diffuse reflectance spectra (UV–Vis) were obtained on a spectrophotometer ((Lambda 1050+, Perkin Elmer, USA) using $BaSO_4$ as a reflectance standard. Room-temperature photoluminescence (PL) spectra were detected on a spectrometer (LS55, Perkin Elmer, USA).

2.7. Photocatalytic CO_2 reduction experiments

The photocatalytic CO_2 reduction experiments were conducted in a sealed reactor system (450 mL) with a top window of quartz glass (Beijing China Education Au-Light Technology., LTD). The reaction temperature was controlled at 0 °C by circulation of ice-water mixture. A 300 W Xe-lamp was placed on top as the light source. For liquid–gas-solid reaction system, the photocatalyst (7 mg) was dispersed into the solvent mixture of acetonitrile (MeCN, 8 mL), triethanolamine (TEOA, 1 mL) and H_2O (3 mL). The reactor was continuously purged with high purity CO_2 with a rate (40 mL/min) for 30 min to remove air and create an oxygen-free environment prior to illumination. The gaseous products at different reaction time were detected by a gas chromatograph equipped with a flame ionization detector (FID) and a thermal conductivity detector (TCD). Liquid chromatography-mass spectrometry (LC-MS) was employed for the identification of potential liquid reduction products.

Notably, the reduction of CO_2 to CO is a 2-electron process, whereas the reduction of CO_2 to CH_4 involves an 8-electron transfer. Consequently, the electron selectivity for CO was calculated according to the

equation below, in which R (CO) and R(CH_4) refer to the formation rates of the gas products CO and CH_4, respectively.

$$\text{Electron selectivity of CO} = 2R(CO)/[2R(CO) + 8R(CH_4)]x100\%$$

2.8. Photoelectrochemical measurements

Transient photocurrent response (i-t), electrochemical impedance spectroscopy (EIS) and Mott-Schottky (M−S) plots were carried out using an electrochemical workstation (CHI 660E Chenhua) with a three-electrode cell. There are a Pt foil counter electrode and a saturated Ag/AgCl reference electrode. The working electrode was prepared by the dip-coating method. The photocatalyst (5.0 mg) was dispersed in Ethanol absolute (0.9 mL) and Nafion (0.1 mL) mixed solution to form a slurry. Next, the slurry (100 μL) was dip-coated on an FTO conductive glass (1.5 × 1.5 cm^2). Subsequently, the film was dried in a vacuum oven at 80°C for 6 h. Re-distilled water solution of Na_2SO_4 (0.1 M) was used as the electrolyte.

3. Results and discussion

The TEM images revealed the ultra-thin 2D sheet morphology of Ni-BDC (Fig. S1a) and CQDs evenly distributed on the sheets of Ni-BDC in 0.45 %CQDs/Ni-BDC (Fig. S1b). Fig. 1 was the XRD spectra of CQDs, Ni-BDC, 0.15 %CQDs/Ni-BDC, 0.30 %CQDs/Ni-BDC, 0.45 %CQDs/Ni-BDC and 0.60 %CQDs/Ni-BDC. The XRD patterns of CQDs showed a broad peak (002) centered at approximately 27°, which was consistent with the previously reported patterns of CQDs[35]. The diffraction peaks of as-prepared Ni-MOF and CQDs/Ni-BDC hybrids at 8.7°, 11.1°, 15.6°, 18.1° and 23.7° corresponded to the (100), (010), (101), (210) and (020) crystal facets of the reported 2-D Ni-based MOF ($Ni_3(C_8H_{18}O_4)_2(OH)_2(H_2O)_4$, Ni-BDC), respectively[36,37]. Compared to pure Ni-BDC, the diffraction peak intensity of the (100) crystal facet in CQDs/Ni-BDC was significantly enhanced, while the intensity of the (010) crystal facet was markedly reduced. This finding suggested that Ni-BDC was oriented along the (100) crystallographic direction with the incorporation of CQDs potentially attributed to the separation of layers in 2D Ni-BDC[34]. This observation indicated that CQDs were likely to be embedded between the layers of 2D-Ni-BDC. Furthermore, the crystallinity of CQDs/Ni-BDC was higher than that of Ni-BDC, as demonstrated by the increased absolute intensity of XRD characteristic peaks. The XRD result of CQDs further confirmed that the crystal facet regulation of Ni-BDC was not attributed to the overlapping of the characteristic peaks of CQDs.

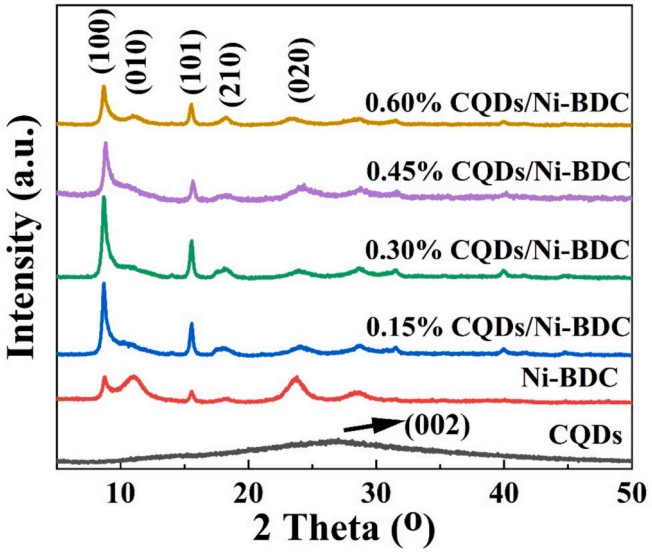

Fig. 1. XRD spectra of CQDs, Ni-BDC, 0.15%CQDs/Ni-BDC, 0.30%CQDs/Ni-BDC, 0.45%CQDs/Ni-BDC and 0.60%CQDs/Ni-BDC.

Fig. 2 was the XPS spectra of Ni-BDC and 0.45 %CQDs/Ni-BDC. The O 1 s spectra of Ni-BDC and 0.45 %CQDs/Ni-BDC could be decomposed into two peaks at 531.9 and 533.9 eV (Fig. 2c), corresponding to the Ni-O bond and the O-C=O bond, respectively. The high-resolution C 1 s spectrum of Ni BDC was divided into three peaks at 285.1 and 288.8 eV, which were assigned to the C–C/C=C and O-C=O bonds, respectively (Fig. 2d)[37]. However, H_2BDC ligand and CQDs had the same carbon species (such as C=C, C–C and O-C=O), which resulted in the signal superposition in the C1s spectrum. Consequently, it was hard to separate the signal peaks of CQDs[38]. The two peaks of Ni 2p at 856.4 and 874.0 eV (Fig.2b) were assigned to 2p3/2 and 2p1/2 of Ni^{2+} for Ni-BDC, respectively. In comparison, the Ni 2p3/2 and 2p1/2 of 0.45 %CQDs/Ni-BDC shifted towards lower binding energy, situated at 856.3 and 873.9 eV, respectively. The alteration in binding energy suggested an increase in the electron density of Ni^{2+}, which could be attributed to the electrons transfer from the electron-rich structure of CQDs[39].The atomic percentage of various elements on the surface and interior (etching for 10 s) of Ni-BDC and 0.45 %CQDs/Ni-BDC was measured by XPS. As presented in Table 1, the C/Ni atomic molar ratio on the Ni-BDC surface was 5.3, which corresponded to the molecular formula. The C/Ni atomic molar ratio on the surface of 0.45 %CQDs/Ni-BDC was 5.8, which was higher than that of Ni-BDC (5.3), indicating the presence of CQDs on the surface. The C/Ni atomic molar ratio at the interface of 0.45 %CQDs/Ni-BDC after 10 s etching was 5.6, which was also higher than that of Ni-BDC (5.2). This result indicated that CQDs also existed between the layers of the 0.45 %CQDs/Ni-BDC hybrid.

The performance of pCO_2RR was evaluated under 300 W Xenon and using TEOA as the sacrificial agent. Almost no H_2 was detected by GC-TCD during the pCO_2RR of Ni-BDC and CQDs/Ni-BDC hybrids (as illustrated in Fig.S2), confirming that no photocatalytic water splitting reaction occurred under the given conditions. GC-FID detection revealed the generation of CO and CH_4 products in pCO_2RR with all photocatalysts, while no other gas product was detected. Furthermore, the use of LC-MS revealed the presence of a single MeCN signal peak, thereby confirming the absence of liquid-phase reduction products (Fig.S3). The data shown in Fig.3 and Table 2 demonstrated that the incorporation of CQDs significantly enhanced pCO_2RR performance. The CO and CH_4 evolution rates of 0.45 %CQDs/Ni-BDC were 0.248 mmol·g^{-1}·h^{-1} and 1.338 mmol·g^{-1}·h^{-1}, respectively. The CO yield rate of 0.45 %CQDs/Ni-BDC was 3.2 times higher than that of pure Ni-BDC (0.077 mmol·g^{-1}·h^{-1}). The electron selectivity of CO_2 reduction towards CO was 97.89 % ($S_{CO} = 2R_{CO}/(2R_{CO} + 8R_{CH4})$, which was the highest of all as-prepared photocatalysts. Compared to other Ni-based MOFs or Ni-MOFs based composites, 0.45 %CQDs/Ni-BDC exhibited better CO product selection (Table S1).

Considering that the products of pCO_2RR might be derived from the decomposition of acetonitrile, TEOA, or the ligands of MOFs. As reported from literature, ^{13}C isotope labeling experiment was generally recognized as one of the most effective approaches for verifying the source of the reduced product[40]. Here, the origin of the reduced products was further confirmed through a series of controlled experiments. As illustrated in Fig. 3d-g, the generation rate of CO was 0.029 mmol·g^{-1}·h^{-1} for without the catalyst, while no CH_4 was observed. This finding is consistent with the literature indicating that the sacrificial agent TEOA possessed photocatalytic capabilities for CO_2 reduction under the ultraviolet light [41]. In the pCO_2RR test of 0.45 %CQDs/Ni-BDC without TEOA, the production rates of CO and CH_4 were determined to be 0.098 mmol·g^{-1}·h^{-1} and 1.207 μmol·g^{-1}·h^{-1}, respectively. The CO yield rate of 0.45 %CQDs/Ni-BDC (0.248 mmol·g^{-1}·h^{-1}) with TEOA was found to be significantly higher than the combined yields (0.029 + 0.098 = 0.127 mmol·g^{-1}·h^{-1}) observed in the two control experiments. This result indicated that the products of pCO_2RR for 0.45 %CQDs/Ni-BDC originated from the photoreduction of CO_2 rather than the decomposition of acetonitrile, TEOA, and ligands.

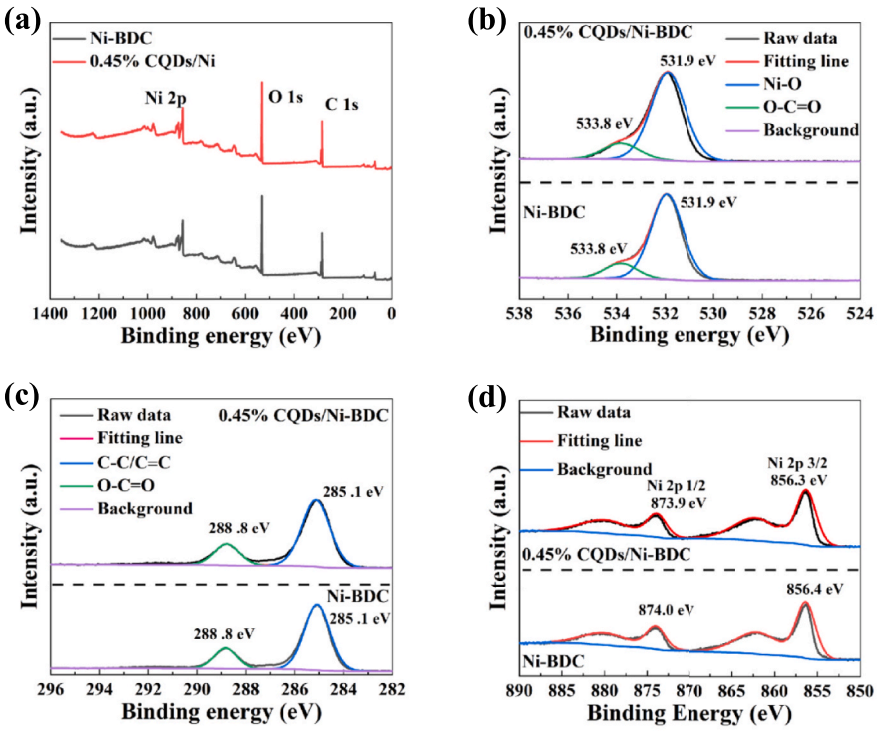

Fig. 2. (a) XPS spectra of Ni-BDC and 0.45 %CQDs/Ni-BDC; (b-d) O 1 s, C 1 s, Ni 2p, deconvoluted spectra of Ni-BDC and 0.45 %CQDs/Ni-BDC.

Table 1
The atomic percentages of various elements in Ni-BDC and 0.45%CQDs-Ni-BDC measured from the XPS spectra.

Sample	Ni (%)	O (%)	C (%)	C/Ni
Ni-BDC (surface)	9.95	36.92	53.13	5.3
0.45 %CQDs/Ni-BDC (surface)	9.29	36.42	54.29	5.8
Ni-BDC (etch 10 s)	12.44	22.71	64.85	5.2
0.45 %CQDs/Ni-BDC (etch 10 s)	11.85	21.79	66.36	5.6

Table 2
The photocatalytic evolution of CO and CH_4 over Ni-BDC and CQDs/Ni-BDC hybrids.

Samples	CO ($mmol \cdot g^{-1} \cdot h^{-1}$)	CH_4 ($\mu mol \cdot g^{-1} \cdot h^{-1}$)	CO Selectivity (%)
Ni-BDC with TEOA	0.077	1.222	94.02 %
0.15 %CQDs/Ni-BDC with TEOA	0.079	3.659	84.38 %
0.30 %CQDs/Ni-BDC with TEOA	0.103	1.806	93.43 %
0.45 %CQDs/Ni-BDC with TEOA	0.248	1.338	97.89 %
0.60 %CQDs/Ni-BDC with TEOA	0.127	2.568	92.53 %
with TEOA but no photocatalyst	0.029	0	100 %
0.45 %CQDs/Ni-BDC without TEOA	0.098	1.207	95.29 %

It is noteworthy that the structure of Ni-BDC underwent decomposition and dissolution in the test system after 6 h of pCO_2RR (Fig. S4a). In contrast, 0.45 %CQDs/Ni-BDC remained original powder after the photocatalytic reaction (Fig.S4b). 0.45 %CQDs/Ni-BDC showed more structural stability in the pCO_2RR compared to Ni-BDC, which may be ascribed to the improved crystalline of the CQDs/Ni-BDC hybrids. To further verify the photocatalytic stability of 0.45 %CQDs/Ni-BDC, multi-cycling pCO_2RR tests were conducted. As shown in Fig. 4, the generation rates of CO over 0.45 %CQDs/Ni-BDC exhibited a continuous decline from the 1st cycle to the 5th cycle test, with the result of the 4th cycle (0.101 $mmol \cdot g^{-1} \cdot h^{-1}$) and the 5th cycle (0.102 $mmol \cdot g^{-1} \cdot h^{-1}$) closely resembling that obtained in the absence of TEOA (0.098 $mmol \cdot g^{-1} \cdot h^{-1}$). The decline of the photocatalytic performance mostly due to the consumption of TEOA with the cycling process. Prior to the 6th cycle of testing, TEOA (1 mL) and H_2O (2 mL) were introduced, the generation rate of CO was raise to 0.26 $mmol \cdot g^{-1} \cdot h^{-1}$. This also proved the stability of smaple 0.45 %CQDs/Ni-BDC. Furthermore, the results from multiple-cycling experiment also demonstrated that the photocatalytic reduction products of 0.45 %CQDs/Ni-BDC did not originate from the decomposition of ligands.

Diffuse-reflectance UV–vis spectroscopy was used to examine the optical response of Ni-BDC and CQDs/Ni-BDC hybrids. As shown in Fig.5a, the CQDs/Ni-BDC hybrids exhibited a higher visible light absorption in comparison to the Ni-BDC, which is presumably attributable to the upconverted circularly polarized luminescence characteristics of the CQDs[42]. The charge migration efficiency of CQDs/Ni-BDC were further verified by a series of characterization techniques, including photoluminescence (PL), electrochemical impedance spectroscopy (EIS) [43] and photocurrent response (Fig.5b-d). Compared to Ni-BDC, the CQDs/Ni-BDC hybrids showed a reduced PL intensity, thereby demonstrating the formation of CQDs/Ni-BDC heterojunction construction. Notably, 0.45 %CQDs/Ni-BDC exhibited the lowest PL peak intensity, smallest charge transfer impedance (Table S2), and highest photocurrent intensity, indicating its superior carrier generation and migration performance, consistent with the results of pCO_2RR tests.

To investigate the effect of crystal facet regulation on the CO_2 reduction performance of CQDs/Ni-BDC, we synthesized CQDs combined with Ni-BDC using a two-step method as a comparison sample named as 0.45 %CS-2. As shown in Fig. 6a, CQDs failed to regulate the crystal facet of Ni-BDC in the 0.45 %CS-2. The production rate of CO for 0.45 %CS-2 was 0.128 $mmol \cdot g^{-1} \cdot h^{-1}$, which was higher than that of Ni-

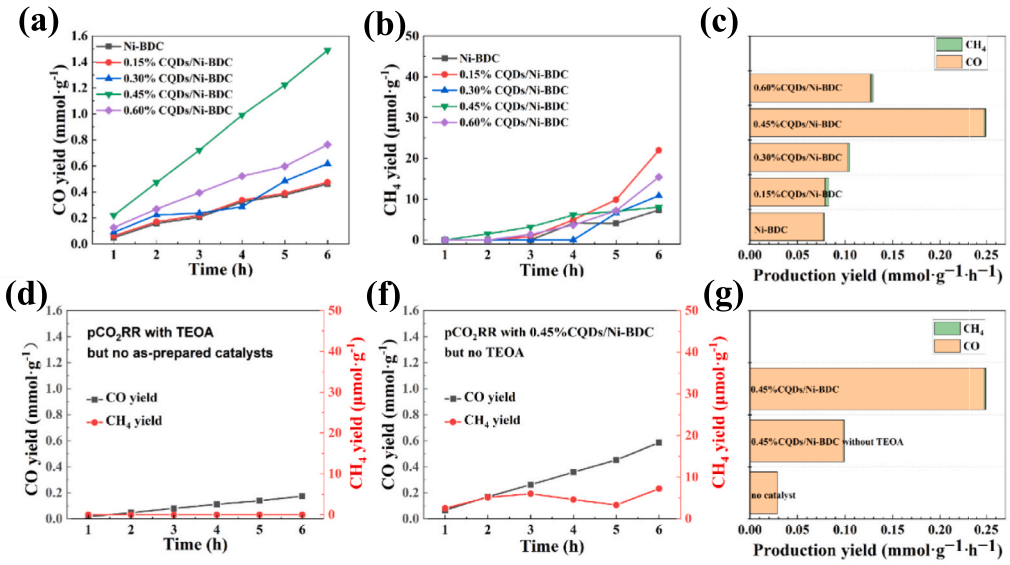

Fig. 3. (a-c) photocatalytic conversion results of Ni-BDC and CQDs/Ni-BDC hybrids: (a) rates of CO generation; (b) rates of CH_4 generation; (c) comparison of the photocatalytic conversion rates of CO_2 to CO and CH_4; (d-g) photocatalytic conversion results of the control experiments: (d) without photocatalyst; (f) 0.45%CQDs/Ni-BDC without TEOA; (g) comparison of the photocatalytic conversion rates of the control experiments and 0.45%CQDs/Ni-BDC (experimental group).

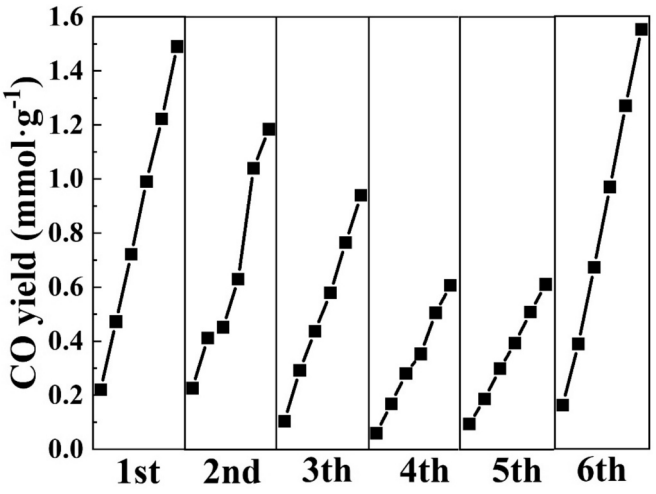

Fig. 4. CO yield rate in the multi-cycling tests of pCO_2RR over 0.45%CQDs/Ni-BDC.

BDC but lower than that of 0.45 %CQDs/Ni-BDC (Fig. 6b and Fig. 6c). This result demonstrated that the exposure of the (100) crystal facet significantly improved the photocatalytic performance of Ni-BDC in pCO_2RR. A possible explanation was that the predominant crystal facet of Ni-BDC changed from (010) to (100), causing some Ni^{2+} to shift from saturated to unsaturated coordination. Additionally, the synergy of two adjacent unsaturated Ni^{2+} sites on the (100) facet reduces the energy barrier for pCO_2RR.[29].

The band structures of Ni-BDC and 0.45 %CQDs/Ni-BDC were analyzed using Tauc-Plot curves and Mott-Schottky measurement. The band gap of Ni-BDC and 0.45 %CQDs/Ni-BDC were estimated as 2.80 and 2.15 eV from the Tauc's-Plot technique by Kubelka-Munk function (Fig.S5) [44]. The flat band positions were determined using Mott-Schottky measurement at various frequencies (500, 1000 and 1500 Hz) in 0.5 M Na_2SO_4. As demonstrated in Fig. 7, the flat band positions of Ni-BDC and 0.45 %CQDs/Ni-BDC were −1.39 and −1.24 V *vs* Ag/AgCl (pH = 7), respectively. Consequently, the LUMO positions of Ni-BDC and 0.45 %CQDs/Ni-BDC separately situated at −1.19 and −1.04 V *vs* NHE (pH = 7), which were more negative compared to the reduction potential of CO_2/CO (−0.53 V *vs* NHE, pH = 7) and CO_2/CH_4 (−0.24 V *vs* NHE, pH = 7)[45]. The migration of photo-generated electrons from the LUMO positions of Ni-BDC and CQDs/Ni-BDC hybrids to CO_2 adsorbed on the active sites for photocatalytic reduction of CO_2 into CO/CH_4 was thermodynamically favorable, while the presence of CQDs significantly improved the efficiency of electron migration.

4. Mechanism analysis

The above analysis suggested that the enhancement of photocatalytic CO_2 reduction performance of the CQDs/Ni-BDC hybrids was attributable to the synergistic effects arising from the CQDs/Ni-BDC heterostructure and the exposure of the (100) crystal facet (Scheme 1). On the one hand, the close interface interaction of CQDs/Ni-BDC heterojunction construction originating from the one-step ultrasonic method facilitated the efficient separation and migration of photogenerated carriers. On the other hand, the crystal facet regulation of Ni-BDC reduced the energy barrier for pCO_2RR as a result of the synergistic effect between two adjacent unsaturated Ni^{2+} ions on the (100) crystal facet.

5. Conclusion

In summary, this work focused on the simultaneous preparation of heterojunction construction and regulation of crystal facets in Ni-based MOFs (Ni-BDC) to synergistically enhance photocatalytic activity for pCO_2RR. XRD results showed that CQDs facilitated the transition of rich (010) crystal facets to the rich (100) crystal facets in Ni-BDC, resulting in a lower energy barrier for pCO_2RR. Compared to Ni-BDC, CQDs/Ni-BDC hybrids showed the more excellent pCO_2RR performance. 0.45 %CQDs/Ni-BDC exhibited the best performance with 0.248 $mmol{\cdot}g^{-1}{\cdot}h^{-1}$ CO and 1.338 $\mu mol{\cdot}g^{-1}{\cdot}h^{-1}$ CH_4 evolution rates and the electron selectivity of CO_2 reduction towards CO was 97.89 %. The CO yield rate of 0.45 % CQDs/Ni-BDC was 3.2 times higher than that of pure Ni-BDC. The PL and photochemical results manifested that the CQDs /Ni-BDC heterojunction construction was successfully synthesized and facilitated the efficient separation and migration of photogenerated carriers, thereby enhancing the utilization of electrons. The combined effect of (100) crystal facet exposure and CQDs/Ni-BDC heterojunction structure

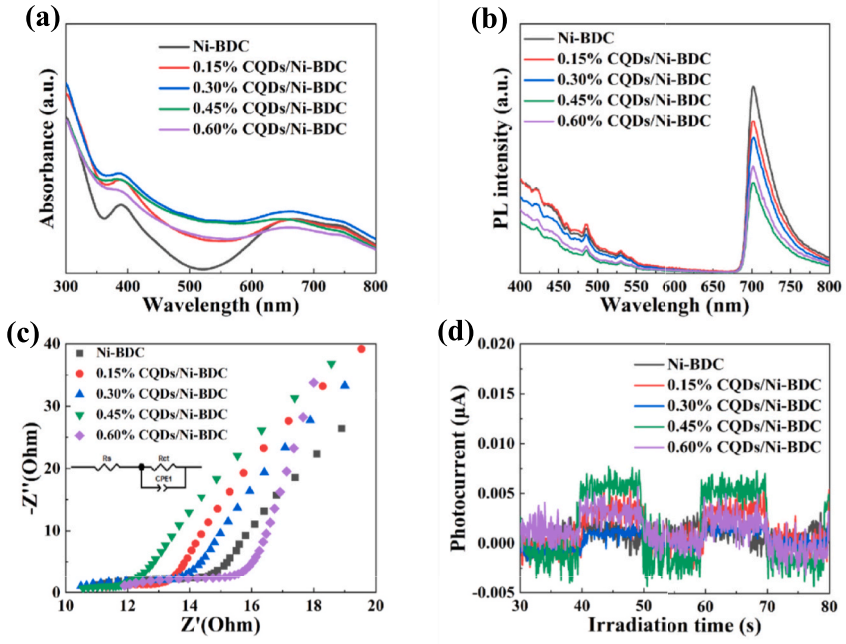

Fig. 5. (a) UV–vis diffuse reflectance spectra; (b) the steady-state photoluminescence (PL) spectra; (c) electrochemical impedance spectroscopy (EIS) plots and (d) photocurrent responses of Ni-BDC and CQDs/Ni-BDC heterojunctions.

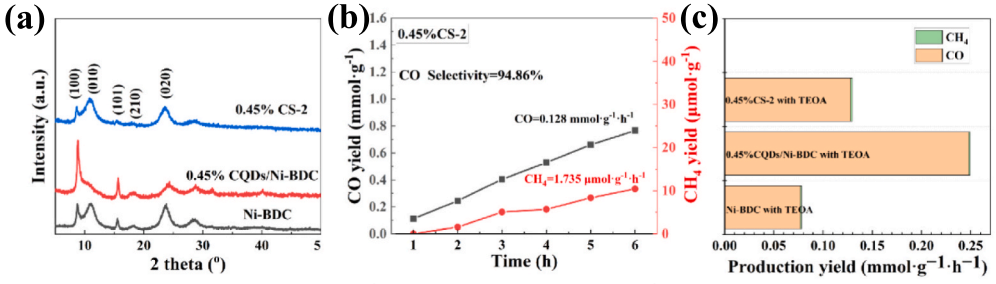

Fig. 6. (a) XRD spectra of Ni-BDC, 0.45%CQDs/Ni-BDC and 0.45%CS-2; (b) photocatalytic conversion results of 0.45%CS-2; (c) comparison of the photocatalytic conversion rates of CO_2 to CO and CH_4.

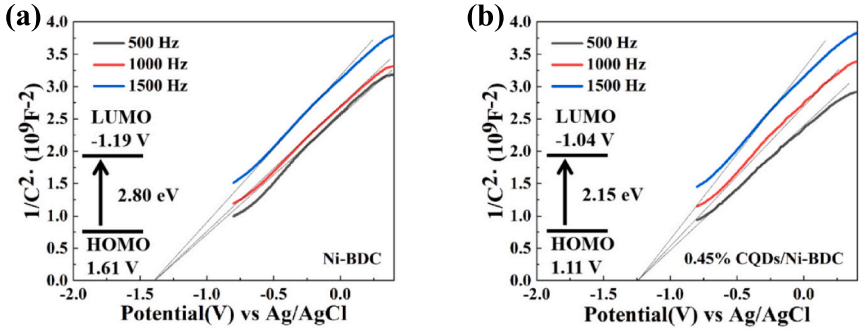

Fig. 7. Mott-Schottky plot of Ni-BDC and 0.45 %CQDs/Ni-BDC in 0.5 M Na_2SO_4 (pH = 7) (Inset: energy diagram of the HOMO and LUMO levels): (a) Ni-BDC; (b) 0.45 %CQDs/Ni-BDC.

synergistically contributed to the enhancement of pCO_2RR performance in CQDs/Ni-BDC.

CRediT authorship contribution statement

Guanhong Lu: Writing – original draft, Methodology. **Xiao Wang:** Investigation, Funding acquisition. **Xinge Li:** Data curation. **Yan Wang:** Methodology. **Gansheng Shi:** Investigation. **Xiaofeng Xie:** Writing –

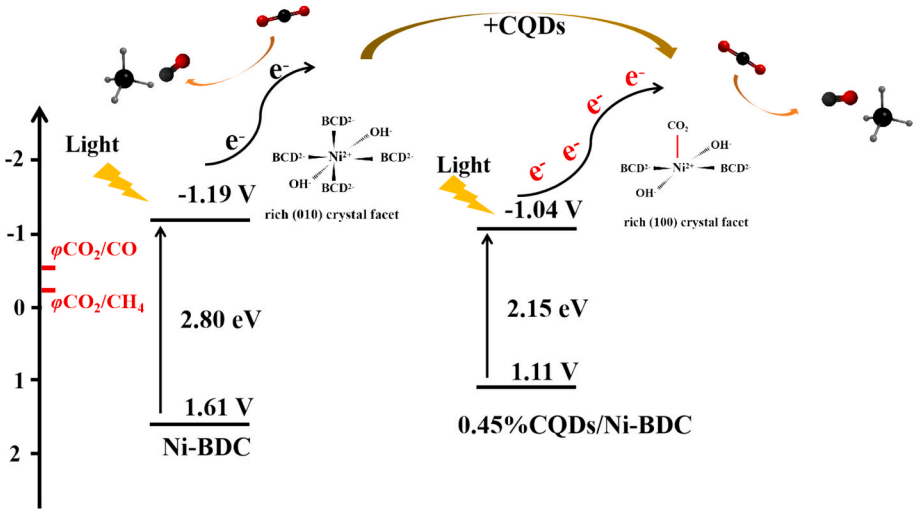

Scheme 1. Schematic illustration of the mechanism of action of CQDs.

review & editing. **Jing Sun:** Writing – review & editing, Supervision, Funding acquisition.

Declaration of competing interest

The authors declare that they have no known competing financial interests or personal relationships that could have appeared to influence the work reported in this paper.

Acknowledgment

This work was financially supported by the National Natural Science Foundation of China (52072387), the Natural Science Foundation of Shanghai (22ZR1471800).

Appendix A. Supplementary data

Supplementary data to this article can be found online at https://doi.org/10.1016/j.apsusc.2025.163647.

Data availability

Data will be made available on request.

References

[1] H.B. Wu, X. Huang, M. Xiao, S.J. Wang, D.M. Han, S. Huang, Thermoplastic polyurethane derived from CO_2 for the cathode binder in li-CO_2 battery, *Nano.* 14 (2024) 1269, https://doi.org/10.3390/nano14151269.

[2] D. Li, C.P. Li, Efficient and reversible capture of CO_2 in CO_2-binding organic liquids formed by 1,1,3,3-tetramethylguanidine and glycerol derivatives, *ACS Sustainable Chem. Eng.* 11 (2023) 5335–5344, https://doi.org/10.1021/acssuschemeng.2c05109.

[3] Y.L. Liu, Z.H. Rui, A storage-driven CO_2 EOR for a net-zero emission Target, *Eng.* 18 (2022) 79–87, https://doi.org/10.1016/j.eng.2022.02.010.

[4] Z. Sun, S. Wang, Q. Li, M. Lyu, T. Butburee, B. Luo, H. Wang, J.M.T.A. Fischer, C. Zhang, Z. Wu, L. Wang, Enriching CO_2 activation sites on graphitic Carbon nitride with simultaneous introduction of electron-transfer promoters for Superior photocatalytic CO_2-to-fuel conversion, *Adv. Sustainable Syst.* 1 (2017) 1700003, https://doi.org/10.1002/adsu.201700003.

[5] C.W. Zhao, Y.F. Guo, J.J. Yan, J. Sun, W.L. Li, P. Lu, Enhanced CO_2 sorption capacity of amine-tethered fly ash residues derived from co-firing of coal and biomass blends, *Appl. Energy* 242 (2019) 453–461, https://doi.org/10.1016/j.apenergy.2019.03.143.

[6] A.M. Cancelliere, F. Puntoriero, S. Serroni, S. Campagna, Y. Tamaki, D. Saito, O. Ishitani, Efficient trinuclear Ru(II)–Re(I) supramolecular photocatalysts for CO_2 reduction based on a new tris-chelating bridging ligand built around a central aromatic ring, *Chem. Sci.* 11 (2020) 1556–1563, https://doi.org/10.1039/c9sc04532e.

[7] R. Zhai, L. Zhang, M. Gu, X. Zhao, B. Zhang, Y. Cheng, J. Zhang, A review of phosphorus structures as CO_2 reduction photocatalysts, *Small* 19 (2023) e2207840, https://doi.org/10.1002/smll.202207840.

[8] M. He, Z. Fang, P. Wang, Y. You, Z.X. Li, Recent Progress in photocatalytic chemical fixation of Carbon dioxide, *ACS Sustainable Chem. Eng.* 11 (2023) 12194–12217, https://doi.org/10.1021/acssuschemeng.3c01994.

[9] X. Liu, T. Chen, Y. Xue, J. Fan, S. Shen, M.S.A. Hossain, M.A. Amin, L. Pan, X. Xu, Y. Yamauchi, Nanoarchitectonics of MXene/semiconductor heterojunctions toward artificial photosynthesis via photocatalytic CO_2 reduction, *Coord. Chem. Rev.* 459 (2022) 214440, https://doi.org/10.1016/j.ccr.2022.214440.

[10] P. Li, Y. Liu, D. Yan, Facts and fictions about photocatalytic CO_2 reduction to C_{2+} products, *ChemSusChem* (2024) e202401174, https://doi.org/10.1002/cssc.202401174.

[11] R. Kuriki, H. Matsunaga, T. Nakashima, K. Wada, A. Yamakata, O. Ishitani, K. Maeda, Nature-inspired, highly durable CO_2 reduction system consisting of a Binuclear Ruthenium(II) complex and an organic semiconductor using visible light, *J. Am. Chem. Soc.* 138 (2016) 5159–5170, https://doi.org/10.1021/jacs.6b01997.

[12] J. Dankar, V. Rouchon, M. Rivallan, C. Pagis, M. El-Roz, Evidence on C-C coupling to acetate as key reaction intermediate in photocatalytic reduction of CO_2 over Pt/TiO_2, *ACS Appl. Mater. Interfaces* 16 (2024) 42210–42220, https://doi.org/10.1021/acsami.4c07256.

[13] L.L. Zhao, J.G. Wang, W.Y. Yang, H.L. Hou, R.F. Yan, Efficient photoreduction of carbon dioxide into carbon-based fuels: a review, *Environ. Chem. Lett.* 21 (2023) 1499–1513, https://doi.org/10.1007/s10311-023-01576-4.

[14] L. Jiang, Z. Li, D. Wang, T. Guo, Y. Hu, In-situ growth of p-type Ag_2O on n-type Bi_2O_2S with intimate interfacial contact for NIR light-driven photocatalytic CO_2 reduction, *Appl. Surf. Sci.* 601 (2022) 154185, https://doi.org/10.1016/j.apsusc.2022.154185.

[15] H. Yin, J. Li, New insight into photocatalytic CO_2 conversion with nearly 100% CO selectivity by CuO-Pd/H_xMoO_{3-y} hybrids, *Appl. Catal., B* 320 (2023) 121927, https://doi.org/10.1016/j.apcatb.2022.121927.

[16] X. Jiang, J. Tan, D. Liu, Y. Feng, K.Q. Chen, E.A. Kazakova, A.S. Vasenko, E. V. Chulkov, Ferroelectric Polarization and single-atom catalyst synergistically promoting CO_2 photoreduction of $CuBiP_2Se_6$, *J. Phys. Chem. Lett.* 15 (2024) 3611–3618, https://doi.org/10.1021/acs.jpclett.4c00687.

[17] H. Xu, H. Song, C. Bi, G. Zhou, X. Liu, K. Zhong, W. Jiang, J. Yang, W. Shen, N. Hao, X. Zhu, H. Xu, X. Wang, X. Zhu, Breaking the intrinsic activity barriers of bilayer metal oxides for catalytic CO_2 reduction, *J. Colloid. Interface Sci.* 675 (2024) 419–428, https://doi.org/10.1016/j.jcis.2024.06.210.

[18] Y. Zhang, M. Cao, H. Feng, D. Liu, Q. Li, Understanding and tuning Charge dynamics in Carbon Nitride/Cobalt(II) complex hybrids for enhanced photocatalytic CO_2 reduction, *ACS Catal.* 13 (2023) 11376–11388, https://doi.org/10.1021/acscatal.3c02945.

[19] Y. Xie, C. Qiu, L. Wang, Y. Wang, J. Zhang, J. Zhang, H. Wan, G. Guan, Microwave-assisted fabrication of 1D/2D CeO_2/Bi_2MoO_6 heterojunction for efficient photocatalytic CO_2 reduction to CH_3OH, *Ceram. Int.* 50 (2024) 25161–25169, https://doi.org/10.1016/j.ceramint.2024.04.245.

[20] H. Yin, F. Dong, D. Wang, J. Li, Coupling cu single atoms and phase junction for photocatalytic CO_2 reduction with 100% CO selectivity, *ACS Catal.* 12 (2022) 14096–14105, https://doi.org/10.1021/acscatal.2c04563.

[21] Y. Huang, K. Wang, T. Guo, J. Li, X. Wu, G. Zhang, Construction of 2D/2D Bi_2Se_3/g-C_3N_4 nanocomposite with High interfacial charge separation and photo-heat conversion efficiency for selective photocatalytic CO_2 reduction, *Appl. Catal., B* 277 (2020) 119232. Doi: 10.1016/j.apcatb.2020.119232.

[22] Y. Yang, Z. Shen, H. Yang, X. Zou, Y. Meng, L. Jiang, Y. Liu, Q. Xia, Y. Cao, X. Li, J. Gao, Y. Wang, Construction adsorption and photocatalytic interfaces between C, O co-doped BN and pd-cu alloy nanocrystals for effective conversion of CO_2 to CO,

J. Colloid. Interface Sci. 640 (2023) 949–960, https://doi.org/10.1016/j.jcis.2023.02.146.
[23] Y. Fu, J. Wu, R. Du, K. Guo, R. Ma, F. Zhang, W. Zhu, M. Fan, Temperature modulation of defects in NH_2-UiO-66(Zr) for photocatalytic CO_2 reduction, *RSC Adv.* 9 (2019) 37733–37738, https://doi.org/10.1039/c9ra08097j.
[24] X.M. Cheng, X.Y. Zhang, X.Y. Dao, S.Q. Wang, J. Zhao, W.Y. Sun, High-index facets exposed on metal-organic framework for boosting photocatalytic carbon dioxide reduction, *Chem. Eng. J.* 431 (2022) 134125, https://doi.org/10.1016/j.cej.2021.134125.
[25] L. Gu, G. Deng, R. Huang, X. Shi, Optimization of Fe/Ni organic frameworks with core-shell structures for efficient visible-light-driven reduction of carbon dioxide to carbon monoxide, *Nanoscale* 14 (2022) 15821–15831, https://doi.org/10.1039/d2nr04377g.
[26] X.Y. Zhang, P. Wang, Y. Zhang, X.M. Cheng, W.Y. Sun, Facet-dependent photocatalytic behavior of fe-soc-MOF for Carbon dioxide reduction, *ACS Appl. Mater. Interfaces* 15 (2023) 3348–3356, https://doi.org/10.1021/acsami.2c19236.
[27] H. Chang, Y. Zhou, S. Zhang, X. Zheng, Q. Xu, CO_2-induced 2D Ni-BDC metal–organic frameworks with enhanced photocatalytic CO_2 reduction activity, *Adv. Mater. Interfaces* 8 (2021) 2100205, https://doi.org/10.1002/admi.202100205.
[28] M. Zhong, X. Li, J. Feng, C. Men, B. Yu, J. Shi, Linker-length dependency of unsaturated ni-oxo clusters in metal hydroxide-organic framework for photocatalytic CO_2 reduction, *Mater. Lett.* 357 (2024) 135669, https://doi.org/10.1016/j.matlet.2023.135669.
[29] W. Yang, H.J. Wang, R.R. Liu, J.W. Wang, C. Zhang, C. Li, D.C. Zhong, T.B. Lu, Tailoring crystal facets of metal-organic layers to enhance photocatalytic activity for CO_2 reduction, *Angew. Chem. Int. Ed.* 60 (2021) 409–414, https://doi.org/10.1002/anie.202011068.
[30] G.U.O. Shao-Ke, C. Kun, H. Hai-Rui, Z. Zhi-Jie, High efficient Carbon quantum Dots/BiOCl nanocomposite for photocatalytic pollutant degradation, *J. Inorg. Mater.* 35 (2019) 491–496, https://doi.org/10.15541/jim20190211.
[31] Y. Hu, X. Xie, X. Wang, Y. Wang, Y. Zeng, D.Y.H. Pui, J. Sun, Visible-light upconversion Carbon quantum dots decorated TiO_2 for the photodegradation of flowing gaseous acetaldehyde, *Appl. Surf. Sci.* 440 (2018) 266–274, https://doi.org/10.1016/j.apsusc.2018.01.104.
[32] W.B. Lv, Y.F. Song, H.B. Pei, Z.L. Mo, Synthesis strategies and applications of metal-organic framework-quantum dot (MOF@QD) functional composites, *J. Ind. Eng. Chem.* 128 (2023) 17–54, https://doi.org/10.1016/j.jiec.2023.07.055.
[33] C. Li, Z. Zhao, X. Wang, M. Li, J. Jiang, S. Dong, Carbon quantum dots induce in-situ formation of oxygen vacancies and domination of 0 0 1 facets in BiOBr microflower for simultaneous removal of aqueous tetracycline and hexavalent chromium, *Chem. Eng. J.* 442 (2022) 136249, https://doi.org/10.1016/j.cej.2022.136249.
[34] H. Wang, P. Zhao, X. Zhang, S. Zhang, X. Lu, Z. Qiu, K. Ren, Z. Xu, R. Yao, T. Wei, Z. Fan, Holey graphene oxide-templated construction of nano nickel-based metal—organic framework for highly efficient asymmetric supercapacitor, *Nano Res.* 15 (2022) 9047–9056, https://doi.org/10.1007/s12274-022-4902-5.
[35] A. Yadegari, J. Khezri, S. Esfandiari, H. Mahdavi, A.A. Karkhane, R. Rahighi, R. Heidarimoghadam, L. Tayebi, E. Hashemi, A. Farmany, Bottom-up synthesis of nitrogen and oxygen co-decorated carbon quantum dots with enhanced DNA plasmid expression, *Colloids Surf., B* 184 (2019) 110543, https://doi.org/10.1016/j.colsurfb.2019.110543.
[36] Y. Xiao, W. Wei, M.J. Zhang, S. Jiao, Y.C. Shi, S.J. Ding, Facile Surface properties engineering of high-quality graphene: Toward advanced ni-MOF heterostructures for high-performance supercapacitor electrode, *ACS Appl. Energy Mater.* 2 (2019) 2169–2177, https://doi.org/10.1021/acsaem.8b02201.
[37] H.W. Zhu, Z. Liu, Z.L. Cheng, Stable dispersed N-doped carbon quantum dots-decorated 2D ni-BDC nanocomposites towards the tribological application, *Appl. Surf. Sci.* 582 (2022) 152428, https://doi.org/10.1016/j.apsusc.2022.152428.
[38] C. Du, Y. Lv, H. Yu, Y. Zhang, H. Zhu, W. Dong, Y. Zou, H. Peng, L. Zhou, X. Wen, J. Cao, J. Jiang, In situ synthesis of oxygen-doped carbon quantum dots embedded in MIL-53(Fe) for efficient degradation of oxytetracycline, *Environ. Sci. Pollut. Res.* 31 (2024) 26686–26698, https://doi.org/10.1007/s11356-024-32729-9.
[39] W. Luo, W. Chen, H. Quan, Z.-X. Zhang, Y. Zeng, Y. Wang, D. Chen, Strongly coupled carbon quantum dots/NiCo-LDHs nanosheets on carbon cloth as electrode for high performance flexible supercapacitors, *Appl. Surf. Sci.* 591 (2022) 153161, https://doi.org/10.1016/j.apsusc.2022.153161.
[40] L.X. Hu, Y. Zhang, Q. Lin, F.Y. Cao, W.H. Mo, S.X. Zhong, H.J. Lin, L.Y. Xie, L. H. Zhao, S. Bai, Unraveling the ni-co synergy in bifunctional hydroxide cocatalysts for better cooperation of CO2 reduction and H2O oxidation in 2D S-scheme photosynthetic systems, *Chin. J. Catal.* 68 (2025) 311–325, https://doi.org/10.1016/S1872-2067(24)60174-9.
[41] Z.G. Liu, J.Y. Li, Z.Y. Chen, M.Y. Li, L.Z. Wang, S.Q. Wu, J.L. Zhang, Photocatalytic conversion of carbon dioxide on triethanolamine: unheeded catalytic performance of sacrificial agent, *Appl. Catal., B* 326 (2023) 122338, https://doi.org/10.1016/j.apcatb.2022.122338.
[42] J. Ke, X.Y. Li, Q.D. Zhao, B.J. Liu, S.M. Liu, S.B. Wang, Upconversion carbon quantum dots as visible light responsive component for efficient enhancement of photocatalytic performance, *J. Colloid. Interface Sci.* 496 (2017) 425–433, https://doi.org/10.1016/j.jcis.2017.01.121.
[43] H.L. Shi, R.W. Shao, S.Y. Lei, M.C. Zhou, X. Yuan, Z.L. Chen, S.Q. Wei, S.X. Zhong, Y.L. Zhao, L.H. Zhao, S. Bai, Breaking Janus shells in hollow heterostructured photocatalysts with spatially separated redox sites for enhanced synergy of CO2 methanation and H2O oxidation, *Appl. Catal. B Environ.* 373 (2025). Doi: doi.org/10.1016/j.apcatb.2025.125363.
[44] H. Srinivasa Varaprasad, P.V. Sridevi, M. Satya Anuradha, Optical, morphological, electrical properties of ZnO-TiO_2-SnO_2/CeO_2 semiconducting ternary nanocomposite, *Adv. Powder Technol.* 32 (2021) 1472–1480, https://doi.org/10.1016/j.apt.2021.02.042.
[45] Z.S. Chen, G.X. Zhang, H.R. Chen, J. Prakash, Y. Zheng, S.H. Sun, Multi-metallic catalysts for the electroreduction of carbon dioxide: recent advances and perspectives, *Renewable Sustainable Energy Rev.* 155 (2022) 111922, https://doi.org/10.1016/j.rser.2021.111922.